International Journal of Biological Macromolecules 335 (2026) 148994

Contents lists available at ScienceDirect

International Journal of Biological Macromolecules

journal homepage: www.elsevier.com/locate/ijbiomac

Collective methodological emission assay of Thioflavin T for qualitative α-synuclein fibril structures discrimination

Grzegorz Szwachta [a,1], Darius Sulskis [b,1], Aleksandra Konopka [c,1], Ewelina Jalonicka [a], Karol Struniawski [c], Kamile Mikalauskaite [b], Andrius Sakalauskas [b], Ryszard Kozera [c], Vytautas Smirnovas [b], Vitali Stsiapura [e], Mantas Ziaunys [b,*], Piotr Hanczyc [a,d,**]

[a] Institute of Experimental Physics, Faculty of Physics, University of Warsaw, Pasteura 5, 02-093, Warsaw, Poland
[b] Institute of Biotechnology, Life Sciences Center, Vilnius University 10257, Vilnius, Lithuania
[c] Institute of Information Technology, Warsaw University of Life Sciences, 02-786, Warsaw, Poland
[d] Center of Cellular Immunotherapies, Warsaw University of Life Sciences, 02-786, Warsaw, Poland
[e] University of Warsaw, Faculty of Chemistry, Żwirki i Wigury 101, 02-089, Warsaw, Poland

A B S T R A C T

α-Synuclein aggregation into distinct fibrillar structures is increasingly recognized as a key determinant of Parkinson's disease heterogeneity, yet rapid discrimination of these morpho-types remains challenging. Here, we present a multi-parametric emission assay, supported by machine-learning, to qualitatively distinguish three α-synuclein fibril samples, containing different fibril structures, which were generated under controlled stressors (temperature, glass-bead surface area, quaking). Atomic force microscopy (AFM) revealed that type I fibrils display cross-sectional height variations, type II form long, flat protofilaments and type III comprise thin fibrils emerging from 40 to 60 nm aggregate clumps. Cryogenic electron microscopy (cryo-EM) confirmed the morphological diversity by showing that each sample contained both single-stranded and double-stranded fibril structures. Time-resolved emission of Thioflavin T (ThT) embedded into α-synuclein fibrils was analyzed using multiexponential and lifetime distribution models. The latter approach via reconstruction of decay lifetime distributions using maximum entropy method demonstrated possibility of fibrils discrimination based on fluorescence decay of ThT and allowed to link the fibrils morphology to emission decay kinetics of the dye. Fabry-Perot cavity lasing was used to confirm samples types discrimination. Automated image analysis of lasing frames using K-nearest neighbors model showed 88 % accuracy in samples type recognition, particularly powerful in recognition of quenched-states of ThT being at play in type III fibrils. The results were compared to fibrils, which were generated using artificial cerebrospinal fluid - a medium that yields a single secondary structure of aggregate filaments. These complementary methodological analyses represent a sensitive platform for α-synuclein fibril structures discrimination, with application in early diagnostic assay.

1. Introduction

α-Synuclein protein predominantly expressed in neuronal tissues, has emerged as the most relevant protein playing a significant role in the pathogenesis of Parkinson's disease (PD) through its propensity to misfold and aggregate [1,2]. α-Synuclein protein is considered as the best clinical biomarker of this disease [3]. In its native state, α-synuclein is implicated in synaptic vesicle regulation and neurotransmitter release [4]. However, under pathological conditions, it undergoes a conformational transition that facilitates the formation of insoluble fibrillar aggregates [5]. Accumulated aggregates are considered to be the pathological hallmark of PD, and are believed to disrupt cellular homeostasis, leading to neurodegeneration [6]. These abnormal aggregates particularly accumulate in neurons in the substantia nigra of the brain but they can also affect other areas of the brain. If protein aggregates accumulate in the bodies of neurons in limbic and cortical areas, they are called Lewy bodies [7]. It is a common feature, but not pathognomonic for PD. Since the substantia nigra produces dopamine, the presence of α-synuclein protein aggregates disrupts this synthesis process. As a result, there is a deficiency of dopamine, which has implications in clinical symptomatology (e.g. bradykinesia, muscle stiffness, resting tremor). The presence of aggregates is also reflected in neuropathological examination (e.g. necropsy examinations) [8].

The precise mechanisms governing α-synuclein aggregation remain an active area of investigation, with evidence suggesting that factors such as post-translational modifications [9], condensation [10], interactions with lipid membranes [11], and stressors may influence its aggregation kinetics [12]. Especially, the last factors - the stressors such

* Corresponding author.
** Correspondence to: P. Hanczyc, Institute of Experimental Physics, Faculty of Physics, University of Warsaw, Pasteura 5, 02-093, Warsaw, Poland.
E-mail addresses: mantas.ziaunys@gmc.vu.lt (M. Ziaunys), piotr_hanczyc@sggw.edu.pl, piotr.hanczyc@fuw.edu.pl (P. Hanczyc).
[1] Authors contributed equally

https://doi.org/10.1016/j.ijbiomac.2025.148994
Received 11 August 2025; Received in revised form 30 October 2025; Accepted 10 November 2025
Available online 11 November 2025

as incubation temperature, surface area of the added glass beads and quaking are stress inducing parameters that can lead to different morphological patterns of fibrils (Fig. 1(a)) [13]. Since it is known that from a chemical point of view, α-synuclein protein can adopt different fibril forms in vitro, this means that this can happen also in vivo in the human brain, where physiological conditions can change as a result of the pathogenesis of the disease, e. g. inflammation and a large number of cytokines associated with this process [14].

2. Materials and methods

2.1. Materials

2.1.1. Thioflavin T

The "UltraPure Grade" compound was obtained from AnaSpec (USA). Two stock solutions were then prepared: a 3.14 mM solution for steady-state and time-resolved fluorescence measurements, and a 78.4 mM solution for lasing experiments.

2.1.2. α-synuclein purification and aggregation

Recombinant α-synuclein was purified based on a previously described protocol [15]. During the final size-exclusion chromatography part, the protein was exchanged into PBS (pH 7.4). The collected protein fractions were then combined, concentrated to 600 μM (ε_{280} = 5960 M^{-1} cm^{-1}) using 10 kDa Pierce protein concentrators (ThermoFisher, cat.no. 88513), distributed to 1.5 mL test-tubes in 500 μL aliquots and stored at −20 °C prior to further use.

Before each protein aggregation procedure, the α-synuclein stock solutions were gently thawed at 4 °C. The aggregation reaction solutions were prepared by diluting the protein stock solutions to a final α-synuclein concentration of 50 μM using 1× PBS (pH 7.4). In order to generate a variety of structurally distinct amyloid fibrils, the aggregation reactions were carried out under a range of different environmental conditions. The protein solutions (500 μL) were placed in 2.0 mL non-binding test-tubes (Axygen™ MaxyClear, cat.no. 11341984). The test-tubes were then incubated at either 25 °C or 37 °C temperature conditions, while being rotated at 10 RPM. Additionally, part of the test-tubes contained 3 mm diameter glass beads to either increase the solution mixing intensity (3 beads / test-tube) or create a large area for surface-induced nucleation (50 beads / test-tube). The aggregation reactions were conducted for 7 days for the 25 °C samples and 3 days for the 37 °C samples. Fibrils formation kinetics are shown in Fig. S1. From each test-tube, 100 μL aliquots were taken for further analysis by FTIR (Fig. S2).

Samples, which possessed unique FTIR spectra and morphologies, were subjected to two rounds of self-replication. 200 μL aliquots of each selected samples were combined with 1800 μL of the initial reaction mixtures. The resulting solutions were then divided into 500 μL aliquots and incubated under their respective initial preparation conditions. This self-replication reaction was done to acquire a larger quantity of each structurally unique sample aggregates for further experimental procedures. The resulting fibril batches were additionally examined by FTIR, AFM and Cryo-EM to determine their differences. All further experimental procedures involved these replicated samples to avoid batch-to-batch variability.

A control sample with well-reproducible structures of α-synuclein fibrils was also made in artificial cerebrospinal fluid (aCSF) (preparation protocol of aCSF in ref. [16]). In short, 50 μM of alpha-synuclein in aCSF solution was placed in 96-well non-binding plates (Corning, 200 μL in each well) and incubated at 37 °C in a ClarioStar Plus plate reader under constant 600 RPM agitation. Each well additionally contained a 3 mm diameter glass bead. The reaction was carried out for 18 h (Fig. S3(a)), after which the fibrils were replicated using the same procedure as described for the previous fibril types. The resulting fibrils were examined by FTIR, Cryo-EM and AFM (Figs. S3(b-e)). Before further experimental procedures, the samples were centrifuged at 14000 xg for 15 min, after which the supernatant was removed and replaced with PBS (pH 7.4). This centrifugation and resuspension procedure was repeated two times in order to replace the aCSF solution. The fluorescence spectra of

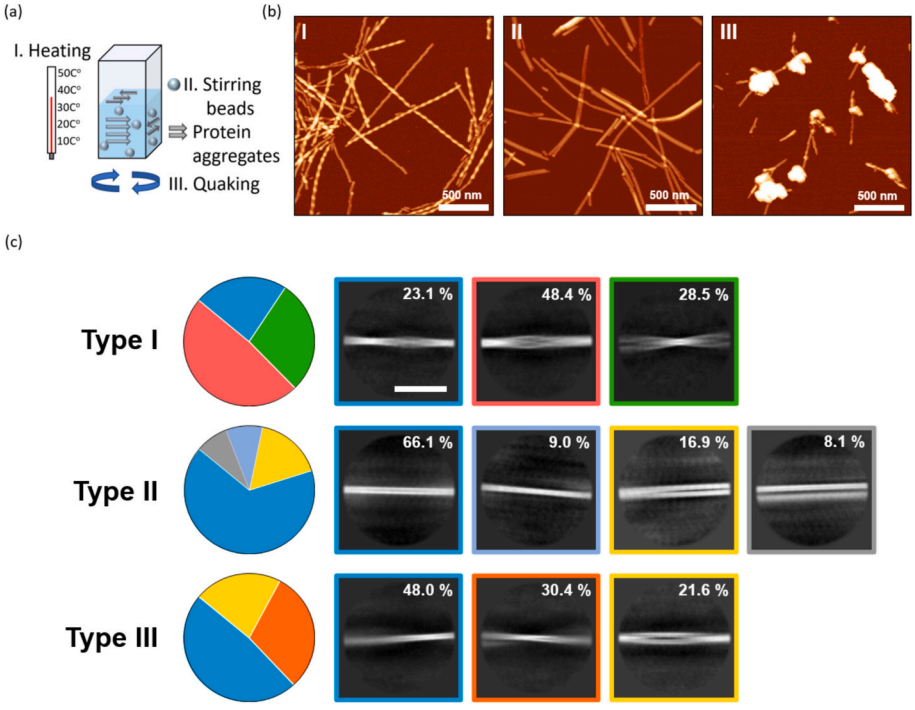

Fig. 1. Morphological and structural characterization of α-synuclein fibrillar structures produced under different external conditions: type I formed at 37 °C, 10 RPM rotation, 0 Beads, type II – 25 °C, 10 RPM rotation, 3 beads, Type III – 25 °C, 10 RPM rotation, 50 beads, (a) schematic illustration of the cuvette with α-synuclein and the external stressors I. temperature, II. surface area of the added glass beads and III. quaking, inducing different morphological patterns of fibrils, (b) AFM images of samples type I, II, III which exhibit distinct molecular structures, (c) Cryo-EM analysis of samples type I, II, III revealed a heterogeneous mixture of fibril classes, including single-stranded (structures in blue box) and double-stranded forms [green, red, gray, orange and yellow boxes](Scale bar is 500 Å).

mature fibrils of four samples are shown in Fig. S4.

3. Methods

3.1. Fourier-transform infrared spectroscopy (FTIR)

Each sample was centrifuged at 14000 x*g* for 15 min, after which the supernatant was removed and replaced with an equal volume of D_2O, supplemented with 400 mM NaCl. The centrifugation and resuspension procedure was repeated three times to completely replace the PBS solution with D_2O. The sample FTIR spectra were then scanned using a Bruker Invenio S FTIR spectrometer, as described previously [17].

3.2. Atomic force microscopy

The selected aggregate samples were diluted to a final protein concentration of 5 μM using 1× PBS. Before fibril deposition, freshly cleaved mica surfaces were modified with (3-aminopropyl)triethoxysilane (APTES). 1 % (% v.v) APTES solution (30 μL) was spread on the surface of the mica, incubated at room temperature for 2 min and then gently washed with 2 mL of H_2O. The mica surface was then dried using airflow. For AFM measurements, 30 μL aliquots of each sample were placed on APTES-modified mica and left to adsorb for 60 s. The mica were then gently washed with 2 mL of H_2O and dried using airflow. AFM measurements were done as described previously using a Dimension Icon atomic force microscope [17]. The acquired AFM images were flattened and analyzed using Gwyddion 2.63 software [18].

3.3. Cryo-EM

For cryo-EM sample preparation, 3 μL of alpha synuclein fibrils were applied to the glow-discharged holey carbon Cu grids (Quantifoil) and blotted with filter paper using Vitrobot Mark IV (FEI Company). The grids were immediately plunge-frozen in liquid ethane and clipped. Cryo-EM data was collected on Glacios transmission electron microscope (Fisher Scientific) operated at 200 kV and equipped with a Falcon IIIEC camera. The micrographs were aligned, motion corrected using MotionCorr2 1.2.1 and the contrast transfer function was estimated by CTFFIND4. The fibrils were picked and subsequent iterations of 2D classifications were performed in Relion 5.0. FilamentTools (https://github.com/dbli2000/FilamentTools) were used to identify the distribution of polymorphs, which is a part of Relion 5.0 software. The data collection and 2D classification details are presented in Supplementary Table 1 (Table S1).

3.4. Steady-state and time-resolved fluorescence spectroscopy

Femtosecond pulses for steady-state and time-resolved fluorescence were produced by frequency-doubling the output of an Orpheus optical parametric amplifier (Light Conversion), itself pumped by a Carbide femtosecond amplifier (Light Conversion), to yield 420 nm excitation at 2 MHz repetition. Emission and excitation spectra were collected in 1 × 1 cm quartz cuvettes on a Horiba QuantaMaster 8075–11 spectrofluorometer, fitted with a PPD850 photomultiplier (250–850 nm sensitivity) and a DeltaTime kit for time-resolved work. Both excitation and emission slit widths were set to 1 nm, and all spectra were corrected for detector sensitivity. Excitation power was kept low enough to prevent detector saturation and preserve linearity. The instrument response function (IRF) with ~230 ps duration (fwhm) was measured by scattering the excitation beam in a TiO_2 suspension. Fluorescence decays were analyzed using multiexponential and lifetime distribution models. Parameters of multiexponential decay were obtained using iterative reconvolution method as implemented in Horiba FelixGX and software package, described previously [19]. The duration of the multiexponential decay kinetics was characterized by using average decay lifetimes values $\langle\tau\rangle_a$ and $\langle\tau\rangle_w$:

$$\langle\tau\rangle_a = \sum_{i=1}^{m}\alpha_i\tau_i \Big/ \sum_{i=1}^{m}\alpha_i$$

$$\langle\tau\rangle_w = \sum_{i=1}^{m}\alpha_i\tau_i^2 \Big/ \sum_{i=1}^{m}\alpha_i\tau_i$$

where the lifetimes were averaged, respectively, by the amplitude and the weight $W_i \sim \alpha_i\tau_i$ of the *i*-th exponential component into emission.

Lifetime distributions of fluorophores $\alpha(\tau)$ with corresponding fluorescence decay function

$$F(t) = \int_0^\infty \alpha(\tau) exp\Big(-\frac{t}{\tau}\Big) d\tau$$

were reconstructed using Maximum Entropy method (MEM) (for details see SI).

3.5. Lasing in cavities

Lasing spectra were obtained with a femtosecond laser operating at 0.5 kHz and delivering 400 μJ pulses. The fundamental output at 800 nm was converted via an optical amplifier to 420 nm for excitation. The cavity mirrors transmitted nearly 100 % between 400 and 450 nm and reflected about 95–99 % over 470–570 nm, peaking at 520–530 nm. When using dye-labeled proteins, cavity thicknesses varied from 8 to 14 μm. Emission from the gain medium was collected along the axis of the excitation beam, and a long-pass filter (cutoff 470 nm) suppressed residual pump light. The filtered lasing output was recorded with a Teledyne Princeton Instruments ProEM Excelon camera.

3.6. Machine vision

The analysis commenced with the extraction of frames exhibiting the lasing effect. An iterative approach was employed, systematically examining each frame. The input data consisted of *.spe* files containing raw image data acquired from CCD cameras, each comprising 200 frames. Every frame underwent analysis to determine the presence of the lasing effect. This verification process involved applying tailored image preprocessing filters and integrating statistical measurements to enhance detection accuracy. The computational analysis yielded optimized threshold values, ensuring robust identification of the lasing effect across frames. Upon locating all relevant frames, the algorithm extracted the first lasing occurrence and conducted analysis to characterize key features defining the lasing phenomenon.

The first frames exhibiting the lasing effect were subjected to a feature extraction process, which identifies and characterizes the most prominent lasing region within each analyzed frame. The features describing the first frame with lasing effect are as follows:

- The largest object area (pixels) - the total number of pixels comprising the lasing region,
- Average intensity of the largest object - the mean pixel intensity within the lasing region,
- Normalized average intensity - the ratio of the lasing region's average intensity to the mean intensity of the entire image,
- Largest object width (pixels) - the horizontal extent of the lasing region,
- Largest object height (pixels) - the vertical extent of the lasing region,
- Largest object X - the horizontal coordinate of the most prominent lasing region, serving as the wavelength reference,
- Largest object Y - the vertical coordinate, representing the lasing angle, where a value of 512 corresponds to 0° (the center of the image),
- Laser energy (measured in μJ) - corresponds to each frame within the 200-frame dataset.

These features were normalized to ensure consistent scaling, which is critical for both visualization and machine learning-based classification tasks. Normalization transforms data into a uniform range (e.g., [0,1]), preventing features with larger magnitudes from dominating distance-based algorithms (e.g., KNN) or gradient descent optimization. Specifically, min-max normalization was applied, rescaling each feature using the formula: $x_{norm} = \frac{x - x_{min}}{x_{max} - x_{min}}$ where x is the original value and x_{min}, x_{max} are the minimum and maximum values of the features respectively.

The highest classification accuracy was achieved using Laser Energy as the sole input feature in a machine learning-based classification approach. This approach aimed to evaluate whether AI methods could effectively distinguish between different groups of fibrils. The selected classifiers included K-Nearest Neighbors (KNN) [20], Support Vector Machine (SVM) [21], Random Forest (RF) [22] and XGBoost (XGB) [23]. The models were evaluated with the following parameters: KNN with k values ranging from 1 to 10, Random Forest (RF) with the number of trees varying between 100 and 500, SVM with the regularization parameter C ranging from 0.8 to 2.6, and XGBoost (XGB) with *n_estimators* between 100 and 500. The highest classification accuracies achieved using *Pump Laser Energy* for the three classes classification problem were 0.88 for KNN ($k = 3$), 0.8 for SVM ($c = 2.4$), 0.86 for RF ($n = 100$) and 0.84 for XGB (*n_estimators* = *100*), based on the tested parameter ranges.

Subsequently, we evaluated the feasibility of classification using only features extracted from spectroscopy images, excluding Laser Energy. The best classification results for the tested parameter ranges were 0.47 for KNN ($k = 2$), 0.44 for SVM ($c = 2.6$), 0.46 for RF ($n = 450$) and 0.45 for XGB (*n_estimators* = *300*). These results indicate that the fibril groups are challenging to separate based solely on image-derived features. Among the tested methods, KNN demonstrated the highest performance, with class III remaining the most distinguishable (precision = 0.78 for KNN); however, its recall was considerably lower (0.32), highlighting the difficulty in consistently identifying this class. These findings confirm that while fibril classification is possible using image-based features, the achieved accuracy is significantly lower compared to models incorporating *Laser Energy*, underscoring the importance of this feature in distinguishing fibril groups.

To enhance classification and facilitate feature visualization, three feature selection techniques were applied: SelectKBest [24], Recursive Feature Elimination (RFE) [25] and XGBoost Feature Importance [23]. However, none of these approaches led to an improvement in classification accuracy.

4. Results and discussion

To conduct ThT fluorescence assays on structurally distinct fibril samples, it was first necessary to generate these diverse aggregate assemblies. Based on previous observations, where environmental factors played a critical role in determining the end-point fibril structures of α-synuclein, a large variety of conditions were used [5]. In result of applying different external factors (Fig. 1(a)), three morphologically different α-synuclein fibril samples (Fig. S5) were produced and replicated to increase their quantity: type I formed at 37 °C, 10 RPM rotation, 0 Beads, type II – 25 °C, 10 RPM rotation, 3 beads, Type III – 25 °C, 10 RPM rotation, 50 beads. In Fig. 1(b) atomic force microscopy (AFM) images revealed that type I sample exhibit a visible cross-sectional height variation not seen for type II and type III. Type II is visualized as long flat fibrils which reflect that specific stress inducing parameters create a distinct pathway for fibrils formation before even the elongation phase starts. While both Type I and II sample fibrils are commonly observed during α-synuclein aggregation assays *in vitro* [5] Type III reveals unusually thin fibrils that emanate from spherical aggregate clumps measuring approximately 40–60 nm in diameter not seen before. This pattern indicates a potential nucleation event within the aggregate clumps, from which fibril growth is initiated. These three replicated fibril samples were used for all experimental procedures to avoid batch-to-batch variability.

Next, cryogenic transmission electron microscopy (Cryo-EM) was used to get insights into the fibrils architecture (Fig. 1(c) and Table S1). In type I sample, Cryo-EM analysis revealed the presence of three distinct fibrillar classes: a single-stranded, non-twisting form (23,1 %) and two different double-stranded forms, each present in varying proportions (48.4 % and 28.5 %, respectively). This heterogeneous composition reinforces the notion that even under a singular set of conditions during preparation, multiple fibrillar assembly pathways may be concurrently active. Type II and III fibrils exhibited markedly different structural patterns whereby Cryo-EM revealed mostly two classes of single-stranded pattern in type II (66 % and 9 %, respectively) and one class of single-stranded profile in type III (48 %). Both type II and III also contained double-stranded classes of fibrils (16.9 % in case of II and 21.6 % in case of III). We note that Cryo-EM models are capable of revealing fibrils architectures but some patterns remained undefined and undetected like in case of sample III where aggregate clumps are in excess. A complete set of 2D classes is available in the supplementary data (Figs. S6-S9).

ThT staining is widely recognized as a gold standard for amyloid fibril detection because its fluorescence markedly increases when dye binds within the grooves formed by β-sheets and is confined in fibrillar amyloid structures [19,26–28]. Standard protocols of ThT staining allow quantitative measurements for fibrils of similar structural morphology within a certain concentrations range in assumption that ThT binding sites in the stained fibrils, whose emission is probed, give a good representation of a statistical population of all possible binding sites on fibrils present in the dispersion. This last condition has crucial impact on accuracy and repeatability of fluorescence intensity measurements, especially taking into account non-uniform spatial distribution of ThT binding sites in the dispersion and high light scattering. We did not observe clear and reproducible dependence of ThT intensity on morphology of the studied α-synuclein fibril structures (Fig. S4). We suggest that this is related to the fact that in order to distinguish different types of fibrils morphology using ThT emission one needs to assess relative fluorescence quantum yields (QY) averaged over distribution of the binding sites rather than intensities, which depend both on QY and dye concentration.

From the other side fluorescence decay kinetics does not depend on concentration and is minimally affected by excitation or emission light scattering. Moreover, decay kinetics data contain larger amount of information about the system under study, which is capable to provide complementary insights into the heterogeneity of ThT binding sites along the fibril surface. Therefore, after resolving the structural organization of the fibrils using AFM and Cryo-EM, time-resolved fluorescence spectroscopy measurements were carried out. Emission decay of ThT in all three types of fibrils can be successfully described using bi- or three-exponential models (Table 1). In the case of type I fibrils a good fitting with $\chi^2_\nu \sim 1$ could be achieved using only two exponential components with $\tau_1 \sim 0.4$–0.5 ns and $\tau_2 \sim 1.0$ ns. For types II and III fibrils an additional long-living decay component with $\tau_3 \sim 2.1$–2.4 ns was necessary to include in the data analysis in order to improve fitting of the decay curves (Fig. S10).

Usually, multi-exponential emission decay for a dye bound to a biomolecule is interpreted as presence of multiple types of binding sites for the dye on the macromolecule and difference in the binding sites microenvironments (polarity, steric interactions, microviscosity, access to quenchers, etc.) causes alteration in the dye emission properties. It is well known that ThT shows properties of fluorescent molecular rotors [19,29], i.e. twisted intramolecular charge transfer is the main non-radiative decay process in the excited state of ThT molecule and restriction in intramolecular mobility of the dye due to steric interactions or microenvironment viscosity [30] can result in alteration of ThT decay lifetime by ~3 orders of magnitude (from ~1 ps in aqueous solutions

Table 1
Decay parameters of ThT fluorescence using multiexponential and lifetime distribution models. $\lambda_{ex} = 420$ nm, $\lambda_{em} = 490$ nm.

sample	Fitting range	α_1	τ_1, ns	W_1, %	α_2	τ_2, ns	W_2, %	α_3	τ_3, ns	W_3, %	$\langle\tau\rangle_a$, ns	$\langle\tau\rangle_w$, ns	χ^2_ν
	Single-curve analysis												
Type I	101–292	0.206	0.45	10.0	0.794	1.05	90.0				0.93	0.99	1.12
	101–320	0.252	0.52	14.0	0.748	1.07	86.0				0.93	1.00	1.36
Type II	101–370	0.702	0.47	39.1	0.298	1.71	60.9				0.84	1.22	1.77
	101–370	0.522	0.31	20.3	0.387	1.06	52.3	0.091	2.35	27.4	0.78	1.26	1.21
Type III	101–350	0.745	0.35	43.2	0.255	1.36	56.8				0.61	0.92	1.68
	101–350	0.608	0.25	26.5	0.344	0.91	55.5	0.048	2.13	18.0	0.56	0.95	1.10
	Global analysis												
Type I	101–320	0.091	0.28	2.7	0.887	0.97	92.3	0.021	2.19	5.0	0.93	1.01	1.41
Type II	101–370	0.490		17.7	0.392		49.0	0.118		33.3	0.77	1.25	1.22
Type III	101–350	0.631		30.0	0.326		53.9	0.043		16.1	0.59	0.96	1.13
	Lifetime distribution analysis using MEM												
Type I	101–320	0.117	(0.1–0.6)	5.7	0.877	(0.6–1.6)	93.2	0.006	(1.6–3.0)	1.1	0.93	1.01	1.82
Type II	101–370	0.491		21.8	0.384		46.5	0.125		31.8	0.82	1.27	1.88
Type III	101–350	0.677		35.0	0.284		50.7	0.039		14.3	0.55	0.95	1.45

[31] to ~1 ns while bound to fibrils). Taking into account high heterogeneity of amyloid fibril structures one can expect that many more than 2 or 3 types of binding sites (that can be inferred from Table 1 with multi-exponential decay results) are present on amyloid fibrils for ThT and our inability to detect them is mainly related to low temporal resolution and insufficient data accuracy. Similar situation is considered to be typical for fluorescent labels or probes within complex macromolecular systems, such as biopolymers [32,33], micelles, membranes [34], which are characterized by high spatial heterogeneity and conformation mobility. Fluorescence decay kinetics of fluorophores in such systems is substantially non-exponential, which is caused, on one hand, by heterogeneity of the binding centers and their different microenvironment, and, on the other hand, by dynamical processes, such as structural and solvent relaxation, energy transfer, etc. In this case data analysis methods that can reconstruct continuous lifetime distributions of emitting centers [32,35,36] seem to be more relevant (see below) to describe decay kinetics.

Therefore, from a mathematical point of view the set of decay parameters $\{\alpha_i, \tau_i\}$ obtained during the multiexponential fit might not represent the unique solution with a certain physical meaning, i.e. several sets of parameters $\{\alpha_i, \tau_i\}$ can be found that fit data almost equally well [37]. This non-uniqueness of the fitting parameters $\{\alpha_i, \tau_i\}$ for the single decay curves is demonstrated by results of global analysis when the whole set of decay curves were analyzed using common lifetimes (Table 1). One can see that decay curves can be satisfactorily fitted using quite different set of parameters $\{\alpha_i, \tau_i\}$ with only a minor change in χ^2_ν values. Notably, since values of lifetimes are set common among the data curves during global analysis ($\tau_1 = 0.28$ ns, $\tau_2 = 0.97$ ns, $\tau_3 = 2.19$ ns) only pre-exponential factors α_i account for variation in fluorescence decays which makes it easier to compare ThT kinetics in different types of fibrils.

In type I fibrils the decay component with $\tau_2 = 0.97$ ns dominates in ThT kinetics and accounts for $W_2 \sim 92$ % of the total emission. It is also present in types II and III fibrils, however, its contribution lowers to ~50 %. Decay component with the longest lifetime $\tau_3 = 2.19$ ns that can be attributed to the most tightly-bound ThT molecules with the most restricted mobility shows the highest contribution into emission $W_3 \sim 33$ % for type II fibrils, while in type III fibrils its weight decreases to ~16 %. We suggest that binding of ThT to small aggregate clumps of 40–60 nm in diameter (Fig. 1b (image III)) may be responsible for the short-lived decay component in type III fibrils, where ThT molecules intramolecular mobility is less restricted or intermolecular quenching effects among closely spaced dye molecules contribute to the reduced lifetime [38].

Amplitude-averaged lifetimes $\langle\tau\rangle_a$ for ThT in fibrils, that scale proportional to fluorescence quantum yield, show dependence on fibrils morphology with the largest value $\langle\tau\rangle_a$ ~0.9 ns for Type I fibrils and the lowest ~0.6 ns for the Type III sample (Table 1). It is interesting to note, that values of amplitude-averaged $\langle\tau\rangle_a$ and weight-averaged $\langle\tau\rangle_w$ lifetimes that characterize decay duration for the ensemble of fluorophores do not depend significantly on kind of analysis that has been employed (single-curve or global analyses) (Table 1). They retain their values also in the case when decay kinetics was described using continuous lifetime distribution of the emitting centers (Fig. 2).

The maximum entropy method [33,36,37,39,40] (MEM) was used to reconstruct lifetime distribution $\alpha(\lg\tau)$ of ThT molecules in fibrils. Description of the method used is presented in SI and in ref. [40]. The fluorophores distribution $\alpha(\lg\tau)$ was modeled using a set of 30 exponentials that spanned lifetimes range from 0.1 ns to 3 ns in logarithmic scale (Fig. 2, Figs. S11-S14).

A narrow unimodal distribution $\alpha(\lg\tau)$ with asymmetric shape and peak at ~1.0 ns was found for ThT in type I fibrils (Fig. 2(b)) in good agreement with fitting results using multiexponential model (Table 1). For type II fibrils one can see a broader $\alpha(\lg\tau)$ distribution with peak at ~0.52 ns that spans from ~0.2 ns to 3 ns, while in case of type III fibrils a bimodal distribution was found with maxima at ~0.26 ns and ~ 0.93 ns.

One can see that lifetime distribution analysis using MEM (Fig. 2(b)) allows easy qualitative discrimination of fibrils samples. In the case of aCSF fibrils that form highly reproducible secondary structures, shape of lifetime distribution (Fig. S14 and S15) is very similar to the one observed for Type I fibrils (Fig. 2). According to our measurements ~76 % of the formed aCSF fibrils have double-stranded (ds) morphology and ~ 23 % - single-stranded (ss) morphology. Practically the same ratio of ds to ss structural patterns were found for Type I fibrils, where two patterns of ds morphology (~48 % and 28 %, total 76 %) were present. Therefore, taking into account similarities of lifetime distributions $\alpha(\tau)$ for both aCSF and Type I fibrils we suggest that the peak at ~1 ns in lifetime distributions is related to ThT binding sites localized predominantly on fibrils with ds morphology.

Reproducibility of the proposed approach to reconstruct lifetime distribution should be evaluated using larger experimental data sets, however, at this point we can easily check how consistent are the results of both MEM and global analysis. We can divide lifetimes distribution range (0.1 ns - 3 ns) into 3 parts corresponding to ThT molecules with short-lived ($\tau < 0.6$ ns), medium ($0.6 \text{ ns} < \tau < 1.6$ ns), and long-lived ($\tau > 1.6$ ns) lifetimes and compare fractions of these fluorophores, as well as their contributions into emission, to the results of global analysis (Table 1). Table 1 shows good agreement between results of the both methods. Thus, lifetime distribution analysis allows easy discrimination of fibrils types and could be a powerful tool to monitor fibrillogenesis process.

To further investigate fractional amount of ThT in each environment, lasing experiments were conducted in the condensed phase achieved by tenfold volume reduction using column filters. The enhanced nanoscale effects in highly condensed matter allow for more reliable detection of ThT binding sites heterogeneity and quenching interactions [41]. The

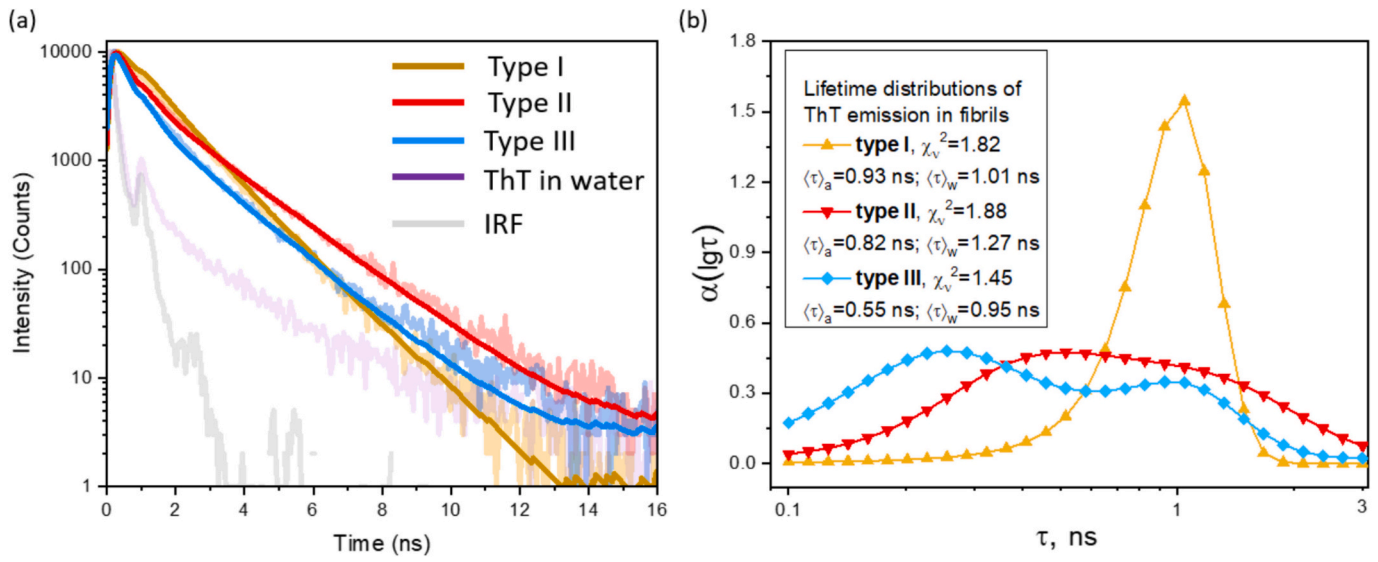

Fig. 2. (a) time-resolved fluorescence decays of ThT-stained α-synuclein fibrils fitted with biexponential function: type I (gold color), type II (red), type III (blue). As a reference ThT in water (violet), IRF (gray). λ_{ex} = 420 nm and λ_{em} = 490 nm, (b) Area-normalized lifetime distributions α(lg τ) of ThT emission in α-synuclein fibrils. 30 exponentials were used to represent lifetime distribution within τ range 0.1–3 ns.

Fabry-Perot cavity lasing technique employs a pair of highly reflective mirrors that serve as photonic resonators, thereby enhances the excitation rate, the radiative part of the decay rate, and the directivity within the confined space of the cavity [42,43]. In this configuration, the ThT-labeled condensed fibril solution acts as the gain medium, where the interaction between the dye and the fibrils facilitates efficient light amplification. Figs. 3(a, b) schematically illustrates the amplification process: once the energy within the cavity surpasses the threshold required for achieving population inversion, a marked transition occurs. This is evidenced by the appearance of a bright emission spot on the camera and the emergence of distinct, narrowband lasing peak (FWHM ~ 2 nm) in the processed emission spectrum (Fig. 3b). The precise pump energy at which this transition is observed is defined as the lasing threshold (Fig. 3c), indicating the critical point where the gain medium's amplification overcomes all losses within the cavity. The lower lasing threshold results from stronger suppression of molecular rotation of ThT's rings caused by binding to different amyloid fibrillar polymorphism, implying the optimal accommodation of the dye. Therefore, lasing threshold was found to enable sensitive detection of subtle protein conformational changes [44]. Precise discrimination of the lasing threshold was enhanced by harnessing the machine learning. Two hundred images were recorded during millimeter stepwise movement of the gray filter allowing rise of the pump energy until the first frame showing lasing occurs. The large number of images requires automation of the image data analysis using machine vision (MV)-based technique. MV methods were employed to compare the results between three fibril samples whereby 33 independent experiments were done for type I, 26 for type II and 22 for type III. In total 16,200 images were recorded. This approach facilitated the large-scale analysis of a significant number of lasing images aiming to the first frame in which lasing occurs, thereby

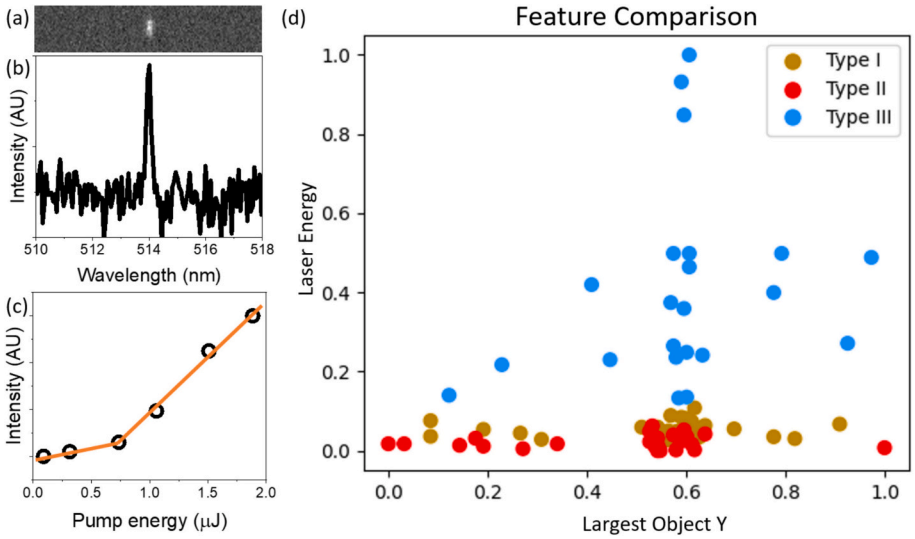

Fig. 3. (a) lasing signal image captured from the Fabry-Perot cavity, where highly reflective mirrors confine the ThT-labeled fibril solution (serving as the gain medium) to achieve light amplification λ_{ex} = 420 nm, (b) representative lasing spectrum displaying distinct, narrowband peak that emerge when the excitation energy exceeds the threshold required for population inversion, (c) example of the lasing threshold determination, illustrating the critical pump energy at which the gain medium's amplification overcomes cavity losses, marked by a bright emission spot and the transition to lasing, (d) scatter plot of two normalized features: Laser Energy and Largest Object Y. Data points are color-coded by fibril type: Type I (gold), Type II (red) and Type III (blue).

determining the lasing threshold for each sample type - a task that would have been impractical for manual analysis due to the large number of images.

The first frames exhibiting the lasing effect were subjected to a feature extraction process (*for details see SI*). The significance of the features was assessed using the Kruskal-Wallis, a non-parametric statistical test to determine whether samples originate from the same distribution. Among the examined features, only Laser Energy and Largest Object Y were statistically significant. In brief, the Largest Object Y is the vertical coordinate, representing the lasing angle, where a value of 512 corresponds to 0° (the center of the image), and Laser Energy corresponds to the energy associated with each frame within the 200-frame dataset. These features were normalized to ensure consistent scaling, making them suitable as input for classification methods (Fig. 3(d)). The highest classification accuracy (0.88) was achieved using Laser Energy as the sole input feature in a machine learning-based approach, with K-Nearest Neighbors [20] (KNN, $k = 3$) outperforming other methods. This demonstrates the potential of MV-driven techniques in distinguishing between fibril samples.

Among the three types, type III exhibited the highest classification performance, as indicated by precision and recall values across all methods. Due to the sensibility of MV-assisted to subtle variation in ThT binding, the fibril sample type III can be accurately distinguished from the other types. This clear separation shows the unique lasing characteristics inherent to type III sample, reflecting specific organization of the ThT dye molecules in 40–60 nm diameter aggregate clumps visualized also by AFM. In contrast, all selected classification methods demonstrated low recall for class II, indicating difficulties in identifying this fibril type, suggesting the appearance of the variety of complex binding mechanisms. When precise identification of class I is a priority, KNN again emerges as the most suitable choice, achieving a recall of 0.97 for this class.

Table 2 provides a numerical overview of the lasing thresholds distribution shown in the Fig. 3d, highlighting notable differences among the samples with type III distinctly requiring a substantially higher excitation energy (4.54 μJ on average) to cross energy thresholds required for lasing compared to type I (0.93 μJ on average) and II (0.62 μJ on average). In addition to these threshold disparities, a spectral shift was observed: the lasing peak for type III appears at approximately 514 nm – about ~ 2 nm red-shifted relative to the average peak positions of samples I and II. The subtle red-shift of emission position is often associated with ThT binding to amyloid fibrils in aggregated forms [45]. The low lasing threshold for types I and II demonstrates that ThT incorporates into amyloid fibrils in the monomeric form in morphologically different α-synuclein fibrillar structures. The agglomeration of ThT mediated by spherical aggregate clumps in type III is not detectable in steady-state fluorescence measurement, but strongly distinguishable by using Fabry-Perot cavity lasing. The maximum of a broad emission band originating from the fluorescence measurement is challenging to locate accurately, which limits the precision of detection. The spectral-shift-based optical sensing is an attractive approach due to the robustness and feasibility originating from the independence of the emission-band position from excitation conditions and local fluctuations in excitation power density. The narrowband nature of lasing signal paves the way for spectral-shift-based sensing of amyloid fibrillar polymorphism of α-synuclein, unveiling the hidden photophysical behavior of ThT dye in the agglomerated state. Given the well-established sensitivity of lasing phenomena to the local microenvironment surrounding ThT dye molecules, these pronounced differences in both lasing thresholds and spectral positions strongly suggest that intermolecular interactions are at play. Specifically, the formation of nanometer-scale α-synuclein aggregate clumps in type III appears to facilitate enhanced quenching mechanisms and promote the aggregation of ThT into nanoaggregates. These unique conditions alter the optical feedback within the cavity, ultimately modulating the lasing characteristics observed for this sample.

Table 2
Lasing parameters in three α-synuclein samples (I, II, II).

Type	Average Lasing threshold (μJ)	Lasing threshold (μJ) range (min. – max.)	Average lasing spectral peak position (nm)
I	0.93	0.66–1.50	512.1
II	0.62	0.41–1.03	512.7
III	4.54	1.75–10.66	514.3

5. Conclusions

In conclusion, a collective methodological emission assay successfully distinguished among distinct α-synuclein fibril samples by leveraging the sensitivity of ThT fluorescence lifetime distributions and Fabry-Perot cavity lasing techniques. The integrated approach combining AFM, TEM, time-resolved fluorescence, and classification applying machine learning for lasing have revealed that subtle differences in fibrillar morphology significantly impact the optical properties of the ThT microenvironment. Notably, the unique lasing characteristics observed for type III show the influence of nanometer-scale protein clustering on intermolecular interactions and quenching mechanisms. These findings enhance the understanding of the molecular heterogeneity associated with α-synuclein aggregation.

To translate this integrated optical assay for discriminating α-synuclein fibril structures into real-world diagnostics, several opportunities and limitations merit emphasis. First, there are technical constraints in a platform that couples fluorescence lifetime measurements with lasing readouts and machine-learning-based classification to resolve structural differences. In the presented current lifetime-distribution analysis, selection of the critical regularization value μ_C is performed manually based on the dependence of the reduced chi-squared, of $\chi^2_\nu(\mu)$. This step should ultimately be automated (analogous to lasing-data workflows). Robust automation will require large datasets comprising ThT-stained fibril decay kinetics paired with lasing-threshold readouts and supported by cryo-EM, enabling accurate, data-driven structural discrimination.

Second, patient-derived aggregates reside in complex milieus (CSF, plasma, vesicles, lipids) and bear post-translational and cofactor signatures that can shift ThT photophysics relative to recombinant samples [46]. Thus, pre-analytical standardization (collection, clarification, freeze-thaw handling, seed amplification) is essential to preserve native heterogeneity while achieving reproducible signal levels. Notably, the Fabry-Perot cavity lasing assay deliberately employs a condensed phase to amplify weak interactions. While this increases sensitivity, it may differentially accentuate nano-aggregation across strains and should be calibrated against orthogonal metrics (e.g., amplitude- and intensity-weighted lifetimes, MEM-derived distributions) to disentangle concentration and scattering effects from intrinsic binding differences.

Transitioning to clinical specificity will further require blinded validation in larger, longitudinal cohorts and cross-laboratory reproducibility across cavity geometries and mirror stacks. Because cryo-EM reveals polymorph mixtures within each preparation, mapping photophysical fingerprints (lifetime modes, lasing spectral shifts, and thresholds) onto defined polymorph proportions in patient samples will likely necessitate joint analyses with seed-amplification products and targeted proteomics to link optical signatures to biochemical determinants. Looking ahead, miniaturized cavities [47] (microfluidic Fabry-Perot cells), multiplexed reporters beyond ThT, and hybrid models that combine lifetime distributions with lasing features could improve robustness while reducing acquisition time. Coupled with standardized aCSF-based references and automated machine-vision analysis, these advances position the approach as a complementary screen for α-synuclein strain heterogeneity and, ultimately, a triage tool to enrich patients for disease-subtype-matched interventions.

CRediT authorship contribution statement

Grzegorz Szwachta: Investigation. **Darius Sulskis:** Writing – review & editing, Investigation. **Aleksandra Konopka:** Software. **Ewelina Jalonicka:** Investigation. **Karol Struniawski:** Software. **Kamile Mikalauskaite:** Investigation. **Andrius Sakalauskas:** Investigation. **Ryszard Kozera:** Supervision. **Vytautas Smirnovas:** Supervision. **Vitali Stsiapura:** Writing – review & editing, Conceptualization. **Mantas Ziaunys:** Writing – original draft, Conceptualization. **Piotr Hanczyc:** Writing – original draft, Supervision, Resources, Investigation, Funding acquisition, Conceptualization.

Declaration of competing interest

I declare no competing interests.

Acknowledgements

Sonata 17 ref. No: 2021/43/D/ST4/01741 granted to P.H. This research was funded by The Research Council of Lithuania, grant number S-MIP-24-52. This work was performed using equipment funded by POIR.04.02.00.00-B003/18. The authors thank the Ministry of Science and Higher Education (Poland) for financial support within the "Support for Polish EuXFEL users – Supervision, Part II (2022–26)" project (agreement No. 2022/WK/13) of the "Support for the participation of Polish teams research in international research infrastructure projects" programme.

Appendix A. Supplementary data

Supplementary data to this article can be found online at https://doi.org/10.1016/j.ijbiomac.2025.148994.

Data availability

Data will be made available on request.

References

[1] J. Burré, R.H. Edwards, G. Halliday, A.E. Lang, H.A. Lashuel, R. Melki, S. Murayama, T.F. Outeiro, S.M. Papa, L. Stefanis, Research priorities on the role of α-Synuclein in Parkinson's disease pathogenesis, Mov. Disord. 39 (10) (2024) 1663–1678.
[2] M. Shahnawaz, A. Mukherjee, S. Pritzkow, N. Mendez, P. Rabadia, X. Liu, B. Hu, A. Schmeichel, W. Singer, G. Wu, Discriminating α-synuclein strains in Parkinson's disease and multiple system atrophy, Nature 578 (7794) (2020) 273–277.
[3] A. Chopra, T.F. Outeiro, Aggregation and beyond: alpha-synuclein-based biomarkers in synucleinopathies, Brain 147 (1) (2024) 81–90.
[4] V. Gao, J.A. Briano, L.E. Komer, J. Burré, Functional and pathological effects of α-synuclein on synaptic SNARE complexes, J. Mol. Biol. 435 (1) (2023) 167714.
[5] M. Ziaunys, A. Sakalauskas, K. Mikalauskaite, V. Smirnovas, Polymorphism of alpha-synuclein amyloid fibrils depends on ionic strength and protein concentration, Int. J. Mol. Sci. 22 (22) (2021) 12382.
[6] C. Toader, C.P. Tataru, O. Munteanu, M. Serban, R.-A. Covache-Busuioc, A. V. Ciurea, M. Enyedi, Decoding neurodegeneration: a review of molecular mechanisms and therapeutic advances in Alzheimer's, Parkinson's, and ALS, Int. J. Mol. Sci. 25 (23) (2024) 12613.
[7] R. Soni, J. Shah, Unveiling the significance of synaptic proteins in Parkinson's pathogenesis: a review, Int. J. Biol. Macromol. 304 (2025) 140789.
[8] T.B. Stoker, J.C. Greenland, Parkinson's Disease: Pathogenesis and Clinical Aspects, 2018.
[9] J.B. Canever, E.S. Soares, N.C. de Avelar, H.I. Cimarosti, Targeting α-synuclein post-translational modifications in Parkinson's disease, Behav. Brain Res. 439 (2023) 114204.
[10] M. Ziaunys, D. Sulskis, D. Veiveris, A. Sakalauskas, K. Mikalauskaite, V. Smirnovas, Diverse effects of fluorescent labels on alpha-synuclein condensate formation during liquid-liquid phase separation, Int. J. Biol. Macromol. 283 (2024) 137688.
[11] A.J. Dear, X. Teng, S.R. Ball, J. Lewin, R.I. Horne, D. Clow, A. Stevenson, N. Harper, K. Yahya, X. Yang, Molecular mechanism of α-synuclein aggregation on lipid membranes revealed, Chem. Sci. 15 (19) (2024) 7229–7242.
[12] M. Ziaunys, A. Sakalauskas, K. Mikalauskaite, V. Smirnovas, Rapid restructurization of conformationally-distinct alpha-synuclein amyloid fibrils at an elevated temperature, PeerJ 10 (2022) e14137.
[13] L. Giehm, N. Lorenzen, D.E. Otzen, Assays for α-synuclein aggregation, Methods 53 (3) (2011) 295–305.
[14] M.G. Tansey, R.L. Wallings, M.C. Houser, M.K. Herrick, C.E. Keating, V. Joers, Inflammation and immune dysfunction in Parkinson disease, Nat. Rev. Immunol. 22 (11) (2022) 657–673.
[15] T. Šneideris, L. Baranauskienė, J.G. Cannon, R. Rutkienė, R. Meškys, V. Smirnovas, Looking for a generic inhibitor of amyloid-like fibril formation among flavone derivatives, PeerJ 3 (2015) e1271.
[16] R. Sniečkutė, D. Šulskis, A. Jocytė, U. Venclovaitė, R. Tamulytė, M. Žiaunys, V. Smirnovas, A. Sakalauskas, Formation of condition-dependent alpha-Synuclein fibril strain in artificial cerebrospinal fluid, bioRxiv (2025), 2025.02.21.639308.
[17] K. Mikalauskaite, M. Ziaunys, V. Smirnovas, Lysozyme amyloid fibril structural variability dependence on initial protein folding state, Int. J. Mol. Sci. 23 (10) (2022) 5421.
[18] D. Nečas, P. Klapetek, Gwyddion: an open-source software for SPM data analysis, Open Phys. 10 (1) (2012) 181–188.
[19] V.I. Stsiapura, A.A. Maskevich, V.A. Kuzmitsky, V.N. Uversky, I.M. Kuznetsova, K. K. Turoverov, Thioflavin T as a molecular rotor: fluorescent properties of thioflavin T in solvents with different viscosity, J. Phys. Chem. B 112 (49) (2008) 15893–15902.
[20] P.K. Syriopoulos, N.G. Kalampalikis, S.B. Kotsiantis, M.N. Vrahatis, K NN classification: a review, Ann. Math. Artif. Intell. (2023) 1–33.
[21] A. Mammone, M. Turchi, N. Cristianini, Support vector machines, Wiley Interdisciplinary Reviews: Computational Statistics 1 (3) (2009) 283–289.
[22] Y. Liu, Y. Wang, J. Zhang, New Machine Learning Algorithm: Random Forest, in: International conference on information computing and applications, Springer, 2012, pp. 246–252.
[23] T. Chen, C. Guestrin, Xgboost: A scalable tree boosting system, in: Proceedings of the 22nd acm sigkdd International Conference on Knowledge Discovery and Data Mining, 2016, pp. 785–794.
[24] R. Nair, A. Bhagat, Feature selection method to improve the accuracy of classification algorithm, Int. J. Innov. Technol. Explo. Eng. 8 (6) (2019) 124–127.
[25] Y. Ding, D. Wilkins, Improving the performance of SVM-RFE to select genes in microarray data, BMC Bioinformatics, Springer, 2006, pp. 1–8.
[26] Y. Miura, S. Namioka, A. Iwai, N. Yoshida, H. Konno, Y. Sohma, M. Kanai, K. Makabe, Redesign of a thioflavin-T-binding protein with a flat β-sheet to evaluate a thioflavin-T-derived photocatalyst with enhanced affinity, Int. J. Biol. Macromol. 269 (2024) 131992.
[27] K. Mikalauskaite, M. Ziaunys, T. Sneideris, V. Smirnovas, Effect of ionic strength on thioflavin-T affinity to amyloid fibrils and its fluorescence intensity, Int. J. Mol. Sci. 21 (23) (2020) 8916.
[28] P. Mudad, D. Alam, B.P. Gurjar, A.S. Kharat, A. Islam, Biophysical and computational insights into glycol-mediated modulation of amyloid dye affinity, Int. J. Biol. Macromol. 320 (2025) 145832.
[29] N. Amdursky, Y. Erez, D. Huppert, Molecular rotors: what lies behind the high sensitivity of the thioflavin-T fluorescent marker, Acc. Chem. Res. 45 (9) (2012) 1548–1557.
[30] P. Hanczyc, Cavity lasing of Thioflavin T in the condensed phase for discrimination between surface interaction and β-sheet groove binding in Alzheimer-linked peptides, J. Phys. Chem. Lett. 15 (37) (2024) 9543–9547.
[31] V.I. Stsiapura, A.A. Maskevich, S.A. Tikhomirov, O.V. Buganov, Charge transfer process determines ultrafast excited state deactivation of thioflavin T in low-viscosity solvents, J. Phys. Chem. A 114 (32) (2010) 8345–8350.
[32] J.R. Alcala, E. Gratton, F. Prendergast, Fluorescence lifetime distributions in proteins, Biophys. J. 51 (4) (1987) 597–604.
[33] M. Vincent, J. Gallay, A.P. Demchenko, Solvent relaxation around the excited state of indole: analysis of fluorescence lifetime distributions and time-dependence spectral shifts, J. Phys. Chem. 99 (41) (1995) 14931–14941.
[34] E. Gratton, T. Parasassi, Fluorescence lifetime distributions in membrane systems, J. Fluoresc. 5 (1) (1995) 51–57.
[35] J.S. Beckwith, C.A. Rumble, E. Vauthey, Data analysis in transient electronic spectroscopy–an experimentalist's view, Int. Rev. Phys. Chem. 39 (2) (2020) 135–216.
[36] J.-C. Brochon, [13] maximum entropy method of data analysis in time-resolved spectroscopy, in: Methods in enzymology 240, Elsevier, 1994, pp. 262–311.
[37] A. Siemiarczuk, B.D. Wagner, W.R. Ware, Comparison of the maximum entropy and exponential series methods for the recovery of distributions of lifetimes from fluorescence lifetime data, J. Phys. Chem. 94 (4) (1990) 1661–1666.
[38] P. Hanczyc, Role of alkali cations in DNA–Thioflavin T interaction, J. Phys. Chem. B 128 (31) (2024) 7520–7529.
[39] P.J. Steinbach, R. Ionescu, C.R. Matthews, Analysis of kinetics using a hybrid maximum-entropy/nonlinear-least-squares method: application to protein folding, Biophys. J. 82 (4) (2002) 2244–2255.
[40] V.I. Stsiapura, O.g.S. Kulakovich, A.A. Maskevich, D.V. Guzatov, H.V. Demir, S. V. Gaponenko e, S.A. Maskevich, Effect of polyelectrolyte spacer thickness on fluorescence decay kinetics of IgG-FITC conjugates near plasmonic silver film, Opt. Spectrosc. 131 (10) (2023) 1418–1430.
[41] K. Rusakov, A. El-Turabi, L. Reimer, P.H. Jensen, P. Hanczyc, Thioflavin T— a reporter of microviscosity in protein aggregation process: the study case of α-Synuclein, J. Phys. Chem. Lett. 15 (2024) 6685–6690.
[42] K. Rusakov, S. Demianiuk, E. Jalonicka, P. Hanczyc, Cavity lasing characteristics of Thioflavin T and Thioflavin X in different solvents and their interaction with DNA for the controlled reduction of a light amplification threshold in solid-state biofilms, ACS Appl Opt Mater 1 (12) (2023) 1922–1929.

[43] C. Gong, X. Yang, S.-J. Tang, Q.-Q. Zhang, Y. Wang, Y.-L. Liu, Y.-C. Chen, G.-D. Peng, X. Fan, Y.-F. Xiao, Submonolayer biolasers for ultrasensitive biomarker detection, Light Sci Appl 12 (1) (2023) 292.
[44] P. Hanczyc, P. Fita, Laser emission of thioflavin T uncovers protein aggregation in amyloid nucleation phase, ACS Photonics 8 (9) (2021) 2598–2609.
[45] A.I. Sulatskaya, A.V. Lavysh, A.A. Maskevich, I.M. Kuznetsova, K.K. Turoverov, Thioflavin T fluoresces as excimer in highly concentrated aqueous solutions and as monomer being incorporated in amyloid fibrils, Sci. Rep. 7 (1) (2017) 2146.
[46] A.J. Espay, A.J. Lees, F. Cardoso, S.J. Frucht, D. Erskine, I.M. Sandoval, L. D. Bernal-Conde, A. Sturchio, A. Imarisio, C. Hoffmann, The α-synuclein seed amplification assay: interpreting a test of Parkinson's pathology, Parkinsonism Relat. Disord. 131 (2025) 107256.
[47] Q. Wang, X. Zhao, Y. Li, Z. Lin, M. Fan, Y. Zhang, X. Wu, Modification-free optofluidic Fabry-Pérot capillary microcavities for ultra-sensitivity biosensing, Sensors Actuators B Chem. 447 (2025) 138798.